communications
materials

ARTICLE

https://doi.org/10.1038/s43246-022-00311-w

OPEN

Qubits based on merons in magnetic nanodisks

Jing Xia[1], Xichao Zhang[1], Xiaoxi Liu[1], Yan Zhou[2] & Motohiko Ezawa[3]✉

A meron is a classical topological soliton having a half topological charge. It could be materialized in a magnetic disk. However, it will become a quantum mechanical object when its size is of the order of nanometers. Here, we propose to use a nanoscale meron in a magnetic nanodisk as a qubit, where the up and down directions of the core spin are assigned to be the qubit states $|0\rangle$ and $|1\rangle$. We first numerically show that a meron with the radius containing as small as 7 spins can be stabilized in a ferromagnetic nanodisk classically. Then, we show theoretically that universal quantum computation is possible based on merons by explicitly constructing the arbitrary phase-shift gate, Hadamard gate, and CNOT gate. They are executed by applying a magnetic field or spin-polarized current. Our results may be useful for the implementation of quantum computation based on topological spin textures in nanomagnets.

---

[1] Department of Electrical and Computer Engineering, Shinshu University, Wakasato 4-17-1, Nagano 380-8553, Japan. [2] School of Science and Engineering, The Chinese University of Hong Kong, 518172 Shenzhen, Guangdong, China. [3] Department of Applied Physics, The University of Tokyo, 7-3-1 Hongo, Tokyo 113-8656, Japan. ✉email: ezawa@ap.t.u-tokyo.ac.jp

Quantum computation is carried out with the use of quantum mechanical states[1–3], where superpositions and entanglements play essential roles. In order to execute arbitrary quantum algorithms, it is enough to construct the $\pi/4$ phase-shift gate, the Hadamard gate, and the controlled-NOT-(CNOT) gate. Namely, universal quantum computation is made possible by these three gates according to the Solovay–Kitaev theorem[4–6].

A fundamental problem is how to construct qubits with the use of actual materials. Attempts have been made in superconductors[7], photonic systems[8], quantum dots[9], trapped ions[10], and nuclear magnetic resonance[11,12]. Recently, qubits based on nanoscale skyrmions have also been proposed[13,14]. It is worth mentioning that skyrmions are typical topological spin textures in magnetic materials with chiral exchange interactions[15–18]. They can be found in both two-dimensional and three-dimensional magnetic nanostructures[17–21] and therefore, are promising candidates for classical and quantum applications based on magnetic materials[13,14,22]. However, the simplest example of a qubit is a single spin, where the up spin is assigned to the quantum state $|0\rangle$ and the down spin is assigned to the state $|1\rangle$. The one-qubit gate operation is executed by applying a magnetic field, where the Rabi precession changes the direction of the spin. The Heisenberg interaction gives a two-qubit gate operation[9,12].

Instead of using an isolated single spin, we focus on the core spin in a nanoscale disk made of a chiral ferromagnet, where the magnetic dipole–dipole interaction (DDI) and the easy-plane magnetic anisotropy force the spin direction to show a clockwise or anticlockwise circular rotation in disk geometry, forming a vortex-like structure called a meron[23–33]. Four typical spin configurations of merons are illustrated in Fig. 1. Due to the Dzyaloshinskii–Moriya interaction (DMI), the degenerated ground states are given by the left-handed merons[30] as shown in Fig. 1a, b, which serve as a classical bit.

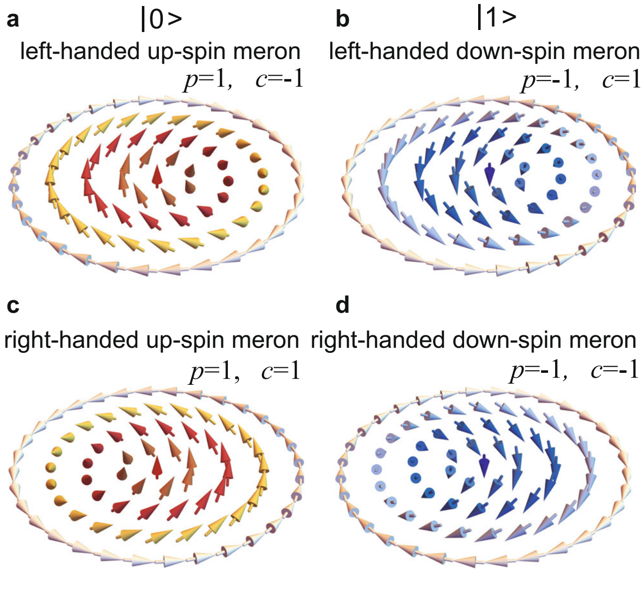

Fig. 1 Schematic illustration of Bloch-type merons. **a** A Bloch-type meron with polarity $p=1$ and chirality $c=1$ representing the qubit state $|0\rangle$. **b** A Bloch-type meron with $p=-1$ and $c=-1$ representing $|1\rangle$. **c** A Bloch-type meron with $p=1$ and $c=-1$. **d** A Bloch-type meron with $p=-1$ and $c=1$. **a** and **b** are the left-handed merons, while **c** and **d** are right-handed merons. The right-handed merons have higher energy than the left-handed merons due to the DMI considered in this work. The arrow represents the spin direction. The out-of-plane spin components are color-coded by the red and blue color scheme: the red arrow points in the $+z$ direction and the blue arrow points in the $-z$ direction.

The meron structure is also a topological spin texture and is topologically protected when the sample size is infinitely large. However, when its size is of the order of 100 nm, it is known to be quite stable and yet to be possible to reverse the core spin. The core-spin direction can be reversed and read out by using a magnetic field[23,26,28] or spin-polarized current[24,25,27]. Hence, a random-access memory has been proposed based on merons[25].

In this work, we propose to use a nanoscale meron in a magnetic nanodisk as a qubit, where it simulates a single spin with a longer relaxation time. First, we study numerically how much the size of a classical meron can be made small. We find that a meron with a radius containing as small as 7 spins are stable by assuming typical material parameters. It is of the order of 3 nm as the lattice constant is 0.4 nm. When the radius of the magnetic nanodisk is of the order of nanometers, the quantum effect will be dominant. A nanoscale meron is uniquely specified by the direction of the core spin. Thus, we assign the up-spin state as $|0\rangle$ and the down-spin state as $|1\rangle$. Their superposition is allowed quantum mechanically, which represents the qubit.

The Zeeman effect due to a perpendicular constant magnetic field induces the Pauli-Z operation to this qubit. By controlling the time duration of the Zeeman field, it is possible to construct an arbitrary phase-shift gate including the $\pi/4$ phase shift gate. Furthermore, by applying an in-plane constant magnetic field, it is possible to flip a spin, which acts as the Pauli-X gate. A sequential application of the Pauli-Z and Pauli-X gates produces the Hadamard gate. Finally, the Ising interaction between layered merons produces the controlled-Z (CZ) gate. A sequential application of the CZ and Pauli-Z gates produces the CNOT gate.

Results and discussion

Classical meron in a chiral magnet. A meron is formed when the spin system has a disk geometry. It is a vortex-like circulating structure of spins, where the spins on the circumference lie within the plane while the core spin points upward or downward, forming the Bloch structure due to the DDI, as illustrated in Fig. 1.

The spin texture located at the coordinate center is parametrized as

$$\boldsymbol{m}(x,y)=(\sin\theta(r)\cos\phi,\sin\theta(r)\sin\phi,\cos\theta(r)),\qquad(1)$$

with

$$\phi=\varphi+\eta+\pi/2,\qquad(2)$$

where φ is the azimuthal angle ($0\leq\varphi<2\pi$) satisfyng $x=r\cos\varphi$, $y=r\sin\varphi$. The polar angle θ is subject to

$$\theta(0)=0,\pi,\qquad\lim_{r\to R}\theta(r)=\pi/2,\qquad(3)$$

where R is the radius of the nanodisk.

A meron is specified by the spin-circulation direction called the chirality $c=\pm1$ and the core-spin direction called the polarity $p=\pm1$. Here, $c=1$ ($c=-1$) for the anti-clockwise (clockwise) rotation, and $p=1$ ($p=-1$) for the up (down) spin. The meron with $cp=1$ is called right-handed and the one with $cp=-1$ is called left-handed.

There are four degenerate merons with $c=\pm1$ and $p=\pm1$ in the absence of the DMI. However, the DMI correlates the polarity and the chirality. The DMI is induced by the inversion symmetry breaking due to the interface between the nanodisk and the substrate[30]. As a result, the left-handed merons are energetically favored[30]. We assign the merons with $p=1$ and $p=-1$ to the classical states $|0\rangle$ and $|1\rangle$, respectively.

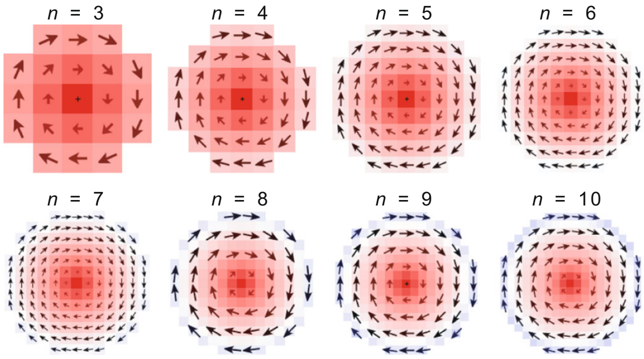

Fig. 2 A simulated state for a meron for radius $n = 3, 4, \cdots, 10$. The in-plane spin direction is indicated by the arrow. The out-of-plane spin component is color-coded: white is in-plane and red is out of the plane. The material parameters used in the simulation are: the exchange constant $A_{\mathrm{ex}} = 0.32$ pJ m^{-1}, Dzyaloshinskii-Moriya interaction (DMI) constant $D = 0.5$ mJ m^{-2}, saturation magnetization $M_s = 152$ kA m^{-1}, and anisotropy constant $K = -0.5$ MJ m^{-3}. More details are given in the "Methods" section.

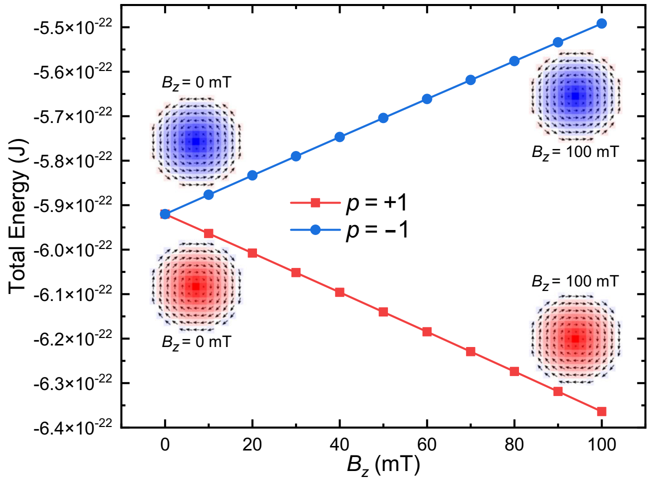

Fig. 3 Total energy of a meron with $p = \pm 1$ as a function of applied perpendicular magnetic field B_z. The radius of a meron is $n = 7$. The simulation parameters are given in the caption of Fig. 2. More details are given in the "Methods" section.

Comments are in order. First, there is a difference from the conventional definition in Eq. (2) by angle $\pi/2$, which makes $\eta = 0, \pi$ correspond to $c = 1, -1$, respectively. Second, $\theta(0) = 0, \pi$ correspond to $p = 1, -1$, respectively, in the boundary conditions (3).

There are two topological numbers defining the meron. One is the skyrmion number,

$$Q \equiv -\frac{1}{4\pi}\int \boldsymbol{m}(\boldsymbol{r}) \cdot (\partial_x \boldsymbol{m}(\boldsymbol{r}) \times \partial_y \boldsymbol{m}(\boldsymbol{r}))\mathrm{d}x\mathrm{d}y, \tag{4}$$

which is given by $Q = p/2$ depending on the polarity p. Note that Q is a half-integer for the meron.

The other is the winding number defined by

$$\omega \equiv \int \left(\boldsymbol{m} \times \frac{\partial \boldsymbol{m}}{\partial \varphi}\right)_z \mathrm{d}\varphi = c, \tag{5}$$

which depends on the chirality c.

It is a nontrivial problem how much the size of a meron can be made small. Let us call it a meron with a radius n when its radius contains n spins. We have performed simulations on the stability of a relaxed static meron with radius n, $n = 3, 4, \cdots, 10$, by embedding it in the $(2n-1) \times (2n-1)$ square lattice, as shown in Fig. 2. The simulations are carried out under the framework of micromagnetics (see the "Methods" section), where we include the ferromagnetic exchange, the DMI, the magnetic DDI, and the easy-plane magnetic anisotropy. As a concrete instance, we have used the material parameters $A_{\mathrm{ex}} = 0.32$ pJ m^{-1}, $D = 0.5$ mJ m^{-2}, and $M_s = 152$ kA m^{-1}. We also considered an in-plane magnetic anisotropy $K = -0.5$ MJ m^{-3}, which favors in-plane spin textures and could assist in stabilizing the meron state. The simulated state of a typical meron is demonstrated in Fig. 2 for $n = 3, 4, \cdots, 10$. We find that a meron is formed for $n \geq 7$.

There are two key features with respect to a meron. One is that a small-size meron is stabilized for a small value of the exchange interaction. It is understood that the exchange interaction becomes large for a large spin angle between the adjacent spins. The spin angle becomes large and the small exchange interaction has an advantage for a nanoscale meron. The other feature is that the large easy-plane magnetic anisotropy stabilizes a nanoscale meron. It is natural because the meron has an in-plane vortex structure except for the core. The radius can be as small as 7 spins. The requirement of the exchange interaction and the easy-plane magnetic anisotropy is relaxed for a larger size of a meron.

Core-spin qubit. We consider a nanodisk in the order of nanometers, where a superposition of the up and down spins is a quantum mechanical state. In this regime, the up and down states of the core spin may act as a qubit. We assign the meron with the up core spin ($p = 1$) as the quantum state $|0\rangle$ and the one with the down core-spin ($p = -1$) as the quantum state $|1\rangle$, as illustrated in Fig. 1. We propose to construct various quantum gates by controlling the meron core spin.

Pauli-Z gate. When we apply an external constant magnetic field B_z along the *z-axis*, the Zeeman effect splits the energy between the up and down spins. The effective Hamiltonian is given by

$$H_z = \alpha_z \sigma_z = \alpha_z(|0\rangle\langle 0| - |1\rangle\langle 1|), \tag{6}$$

where α_z is a constant proportional to B_z. The Pauli-Z gate is constructed by the unitary evolution of H_z, and given by $U_Z = \sigma_z$ (see the "Methods" section).

We have numerically evaluated the energy under such a magnetic field in Fig. 3. The energy difference depending on the polarity is of the order of 10^{-22} J at 100 mT, from which it follows that the operating time is of the order of 1 ps based on Eq. (16).

Pauli-X gate. There are several ways to flip the core spin, such as by applying in-plane magnetic field[34], in-plane oscillating magnetic field[35], currents[24,36,37], rotating magnetic fields[38–40], and spin-polarized current[41,42]. In any case, the effective Hamiltonian is given by

$$H_x = \alpha_x \sigma_x = \alpha_x(|0\rangle\langle 1| + |1\rangle\langle 0|), \tag{7}$$

where α_x is a constant. The Pauli-X gate is constructed by the unitary evolution of H_x, and given by $U_X = \sigma_x$ (see the "Methods" section).

We have numerically analyzed the spin–flip process, by applying an external constant pulse in-plane magnetic field. We see explicitly how each spin rotates to flip the core spin within a meron in Fig. 4. It follows that the switching time of the vortex core direction is of the order of 200 ps.

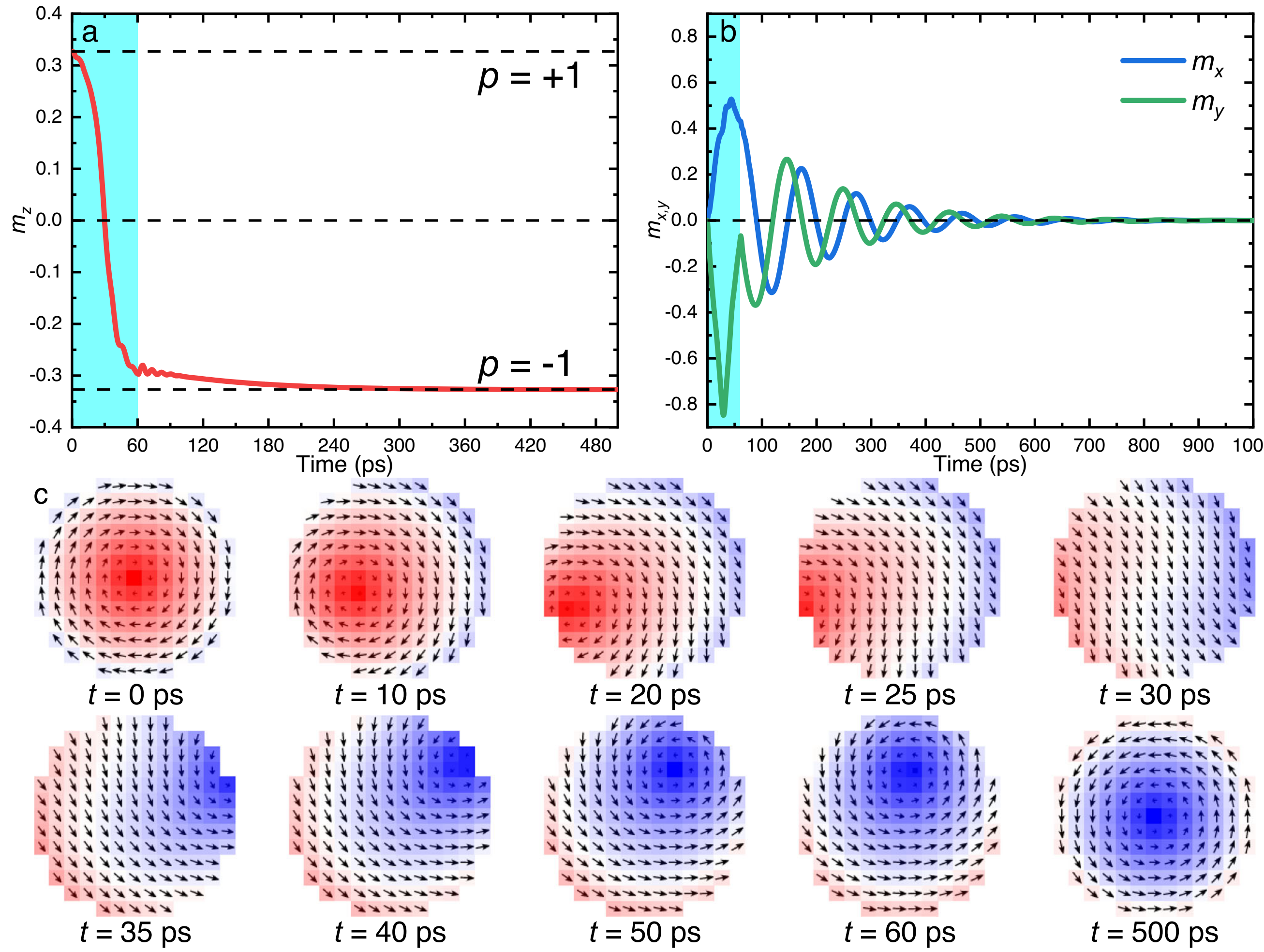

Fig. 4 The switching of the polarity of a meron induced by an in-plane magnetic field pulse. a The out-of-plane component of the reduced magnetization m_z as a function of time. The initial state is a meron ($p = 1$) relaxed in the disk with 13 spins in the diameter (i.e., the radius of the meron is $n = 7$). The in-plane magnetic field of $H_x = 400$ mT is applied for 60 ps (indicated by the cyan area), followed by the relaxation until $t = 1000$ ps. The meron is switched to the state with $p = -1$ after the application of the in-plane field. **b** The in-plane components of the reduced magnetization m_x and m_y as functions of time. **c** Selected top-view snapshots showing the spin configuration in the nanodisk during the field-induced switching of the meron polarity. The simulation parameters are given in the caption of Fig. 2. More details are given in the "Methods" section.

Ising gate. We consider a bilayer nanodisk, where two nanodisks are placed vertically (Fig. 5a). The exchange interaction between two spins reads

$$H_{\text{Ising}} = J_{\text{exchange}} \sigma_z^{(1)} \otimes \sigma_z^{(2)}, \quad (8)$$

where the two nanodisks are placed vertically (Fig. 5a). The Ising gate is constructed by the unitary evolution of H_{Ising}, and given by $U_{ZZ} = \sigma_z^{(1)} \otimes \sigma_z^{(2)}$ (see the "Methods" section).

We have numerically evaluated the energy difference between the identical and opposite polarities, which is ~ 3.6×10^{-22} J. The operating time is ~0.23 ps based on Eq. (25). The detailed energies of the bilayer merons are shown in Fig. 5b.

Universal quantum gates. The phase-shift gate is constructed with the use of H_z. The Hadamard gate is constructed with the use of H_z and H_x. The CNOT gate is constructed with by H_{Ising} and H_z. See the "Methods" section for more details.

Thermal effect. We study thermal stability at finite temperatures. The results are given in Fig. 6. The dynamics of the total m_z are shown in Fig. 6a, where it is seen that the core spin does not flip below 3 K, but flips above 3 K. The time evolution of the Pontryagin number is shown in Fig. 6b. It is stable below 3 K. The time evolution of the spatial profile of the spin configuration is shown in Fig. 6c. The meron texture is destroyed above 3 K. These phenomena correspond to the core spin flipping dynamics in Fig. 6a. Thus, we need to cool down a sample below 3 K.

Relaxation time and coherent time. The skyrmion-number conservation prohibits the core spin to flip when the sample is infinitely large. Then, the relaxation time is infinite. This is topological protection. Physically, it follows from the fact that it costs infinitely large energy to inverse spin directions in an infinitely large sample. The topological protection is lost when the sample size is small. Indeed, when its size is of the order of 100 nm, it is possible to flip the core spin by applying magnetic field[23,26,28] or spin-polarized current[24,25,27].

The two merons representing $|0\rangle$ and $|1\rangle$ are obstructed by an energy barrier made of the exchange energy, easy-plane magnetic anisotropy, and the DDI. We make an estimation for a small-size classical meron based on the energy (9) in the "Methods" section. The size dependence of various energies including the total, exchange, DMI, easy-plane magnetic anisotropy, and magnetic DDI energies is shown in Fig. 7. The total energy increases as the

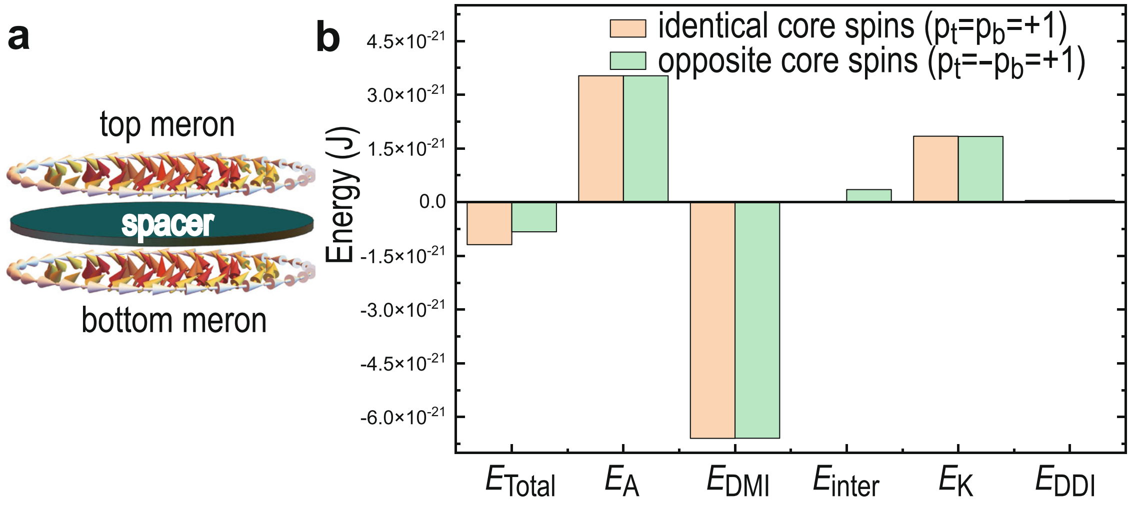

Fig. 5 The Ising interaction between two merons. a Schematic illustration for the Ising interaction between two merons. Dark green cylinders represent a spacer. **b** The contribution of different energy terms to the total energy E_{Total} of a relaxed exchange-coupled bilayer meron with identical or opposite core-spin direction, including the intralayer exchange energy E_{A}, DMI energy E_{DMI}, interlayer exchange energy E_{Inter}, anisotropy energy E_{K}, and dipole–dipole interaction (DDI) energy E_{DDI}. The total energy difference for the exchange-coupled bilayer merons with identical and opposite core-spin directions equals 3.6×10^{-22} J. The radius of the meron is $n=7$, and we have used $A_{\mathrm{Inter}}=0.005$ pJ m^{-1}. The simulation parameters are given in the caption of Fig. 2. More details are given in the "Methods" section.

increase of the meron size as shown in Fig. 7a. The total energy is mainly determined by the exchange energy as shown in Fig. 7b. Roughly speaking, the relaxation time is proportional to the total energy because it is necessary to overcome the total energy to flip the core spin.

There are some features in the size dependence of the energy. The DMI decreases as the increase of meron size as shown in Fig. 7c. It is understood as follows. The DMI is proportional to the spin angles between the adjacent sites. The spin angle is small for larger size merons because the spin texture becomes smooth. As a result, the DMI energy is smaller for larger size merons.

The magnetic anisotropy energy and the DDI energy monotonically increase as the increase of size of a meron as shown in Fig. 7d, e.

The mean magnetization becomes smaller for larger-size merons as shown in Fig. 7f. It means that the size of the core spin is almost identical and the total spin texture looks more like a vortex structure for larger-size merons.

Initialization. We apply a magnetic field to the sample and raise the temperature, where the system is a paramagnet. We have numerically checked that the polarity is chosen to be up by applying a small external magnetic field. When we cool down the sample, left-handed up-spin merons are nucleated. This is the initialization of the quantum state $|00\cdots0\rangle$.

Read out. The polarity can be observed by the full-field soft X-ray transmission microscopy[30,31], magnetic force microscopy[24,43], or magnetic tunneling junction[44]. The polarity is fixed to be up or down by the observation. Hence, the quantum state is fixed to be $\left|s_1 s_2\cdots s_N\right\rangle$ with $s_j=0,1$ as in the standard quantum computation.

Conclusions

We have explicitly analyzed how the Pauli-X, Pauli-Z, and Ising gate operations proceed in a meron-based system. It seems to be a puzzle that the core spin of a meron can be flipped by applying an in-plane constant magnetic field because it is well-known that the spin direction of a ferromagnet cannot be flipped. We have demonstrated how each spin is flipped inside a meron under an in-plane constant magnetic field in Fig. 4. We find that the following process continuously occurs: The spin pointing upward at the core moves to the edge and tilts to the horizontal plane, and then, the spin at the symmetric edge point across the center tilts downward to the south pole and moves to the core.

The numerical estimation suggests that the minimum size of a meron is of the order of 3 nm. The present proposal will excite experimental studies on magnetic nanodisks to pursue how small a nanodisk can be manufactured.

Methods

Simulations of spin configurations. The static spin configurations in the magnetic nanodisk are simulated by using the GPU-accelerated micromagnetic simulator MUMAX3 developed at Ghent University[45]. The energy density of the system is given by

$$\begin{aligned}\mathcal{E} = &-A_{\mathrm{ex}}\sum_{\langle i,j\rangle}\boldsymbol{m}_i\cdot\boldsymbol{m}_j-\sum_i K(\boldsymbol{m}_i\cdot\boldsymbol{e}_z)^2-M_{\mathrm{s}}\sum_i\boldsymbol{B}\cdot\boldsymbol{m}_i\\ &-\mu_0 M_{\mathrm{s}}\sum_i\boldsymbol{m}_i\cdot\tfrac{1}{2}\boldsymbol{H}_{\mathrm{dd}}-\sum_{\langle i,j\rangle}D\boldsymbol{e}_{ij}\cdot(\boldsymbol{m}_i\times\boldsymbol{m}_j),\end{aligned} \tag{9}$$

where $\boldsymbol{m}_i$ represents the local magnetic moment orientation (i.e., $|\boldsymbol{m}_i|=1$), and A_{ex} represents the ferromagnetic exchange constant. K is the easy-plane anisotropy constant, which is a negative number. The axis direction $\boldsymbol{e}_z$ is normal to the easy plane. M_s represents saturation magnetization. $\boldsymbol{B}$ is the applied magnetic field. $\boldsymbol{H}_{\mathrm{dd}}$ is the magnetic-dipole–dipole interaction. The last term represents the bulk DMI with $\boldsymbol{e}_{ij}$ being the unit vector pointing between the lattice site i and j, and D being the magnitude of the DMI, which stabilizes Bloch-type merons. The simulations of spin dynamics at zero and finite temperatures are carried out by using the micromagnetic simulator OOMMF[46], where the spin dynamics at zero temperature is described by the Landau–Lifshitz–Gilbert (LLG) equation

$$\frac{\mathrm{d}\boldsymbol{m}}{\mathrm{d}t}=-\gamma_0\boldsymbol{m}\times\boldsymbol{h}_{\mathrm{eff}}+\alpha\left(\boldsymbol{m}\times\frac{\mathrm{d}\boldsymbol{m}}{\mathrm{d}t}\right), \tag{10}$$

where

$$\boldsymbol{h}_{\mathrm{eff}}=-\frac{1}{\mu_0 M_{\mathrm{s}}}\cdot\frac{\delta\mathcal{E}}{\delta\boldsymbol{m}} \tag{11}$$

is the effective field. α is the Gilbert damping parameter, and γ_0 is the absolute gyromagnetic ratio. The thermal effect is described by the stochastic LLG equation, where a highly irregular fluctuating field $\boldsymbol{h}_{\mathrm{f}}$ is added to the effective field $\boldsymbol{h}_{\mathrm{eff}}$, satisfying

$$\begin{aligned}&\langle h_i(\boldsymbol{x},t)\rangle=0,\\ &\langle h_i(\boldsymbol{x},t)h_j(\boldsymbol{x}',t')\rangle=\frac{2\alpha k_{\mathrm{B}}T}{M_{\mathrm{s}}\gamma_0\mu_0 V}\delta_{ij}\delta(\boldsymbol{x}-\boldsymbol{x}')\delta(t-t'),\end{aligned} \tag{12}$$

where i and j are Cartesian components, k_{B} is the Boltzmann constant, T is the temperature, V is the volume, and δ_{ij} and $\delta(\ldots)$ stand for the Kronecker and Dirac delta symbols, respectively. The finite-temperature simulations are performed with a fixed time step of 2×10^{-15} s, while the time step in zero-temperature simulations is adaptive.

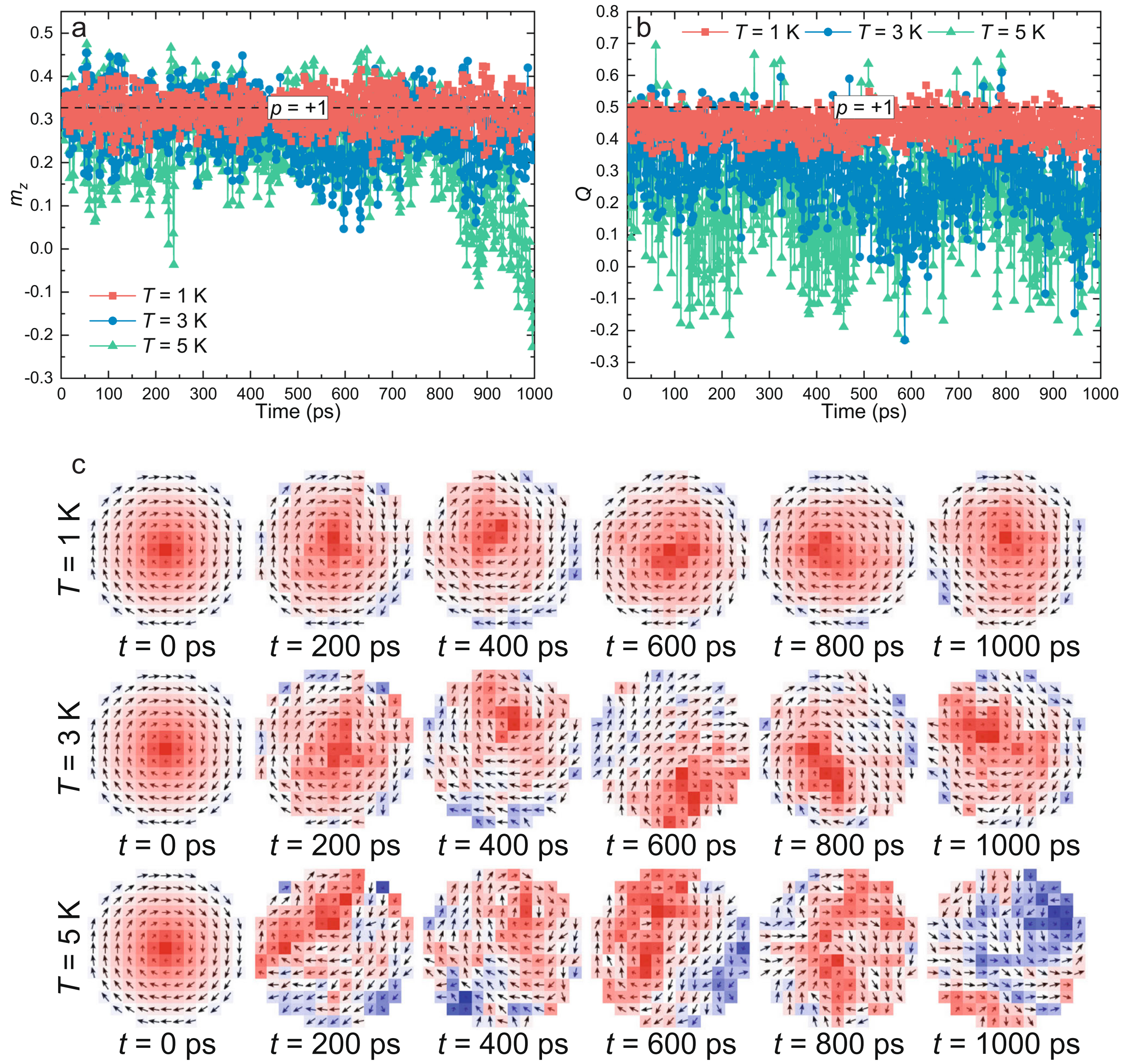

Fig. 6 The meron dynamics at finite temperatures. a The out-of-plane spin component m_z as functions of time at different temperatures T. A relaxed meron with $p = +1$ is placed at the nanodisk with $n = 7$ at $t = 0$ ps. The thermal fluctuations reduce the stability of the meron state. **b** The topological charge of the system Q as functions of time at different temperatures. For a relaxed meron at zero temperature, the topological charge equals 0.5. **c** Selected top-view snapshots of the spin configurations in the nanodisk at different temperatures. The radius of the meron is $n = 7$, and the damping parameter $\alpha = 0.1$. The simulation parameters are given in the caption of Fig. 2. More details are given in the "Methods" section.

The square lattice with a circular shape is used for simulations with the lattice constant being 0.4 nm, i.e., the mesh size is 0.4 nm × 0.4 nm. Open boundary conditions are used for all sample edges. The nanodisk is assumed to be a 1-nm-thick with bulk DMI. The following material parameters are used as default parameters: $A_{\mathrm{ex}} = 0.32\ \mathrm{pJ\ m^{-1}}$, $\alpha = 0.3$, $M_{\mathrm{s}} = 152\ \mathrm{kA\ m^{-1}}$, $D = 0.5\ \mathrm{mJ\ m^{-2}}$, and $K = -0.5\ \mathrm{mJ\ m^{-3}}$.

Construction of quantum gates. The Schrödinger equation for qubits is

$$i\hbar \frac{d}{dt}|\psi\rangle = H|\psi\rangle, \tag{13}$$

with the Hamiltonian

$$H = \alpha_z \sigma_z + \alpha_x \sigma_x \tag{14}$$

for a single qubit, and

$$H_{\mathrm{Ising}} = J_{\mathrm{exchange}} \sigma_z^{(1)} \otimes \sigma_z^{(2)} \tag{15}$$

for two qubits. We control the coefficient B_z, B_x, and J_{exchange} temporally. We first discuss single-qubit gates.

Pauli-Z gate. We set $B_x = 0$ and

$$\alpha_z(t) = \hbar\theta/2t_0 \tag{16}$$

for $0 \le t \le t_0$ and $\alpha_z(t) = 0$ otherwise. The solution of the Schrödinger equation reads

$$U_Z(\theta) = \exp\left[-\frac{i}{\hbar}\sigma_z \int_0^{t_0} \alpha_z(t)\mathrm{d}t\right] = \exp\left[-\frac{\mathrm{i}\theta}{2}\sigma_z\right]. \tag{17}$$

This is the z rotation gate by the angle θ. It gives an arbitrary phase-shift gate

$$U_\theta = \mathrm{e}^{\mathrm{i}\theta/2} U_Z(-\theta) = \mathrm{diag}(1, \mathrm{e}^{\mathrm{i}\theta}). \tag{18}$$

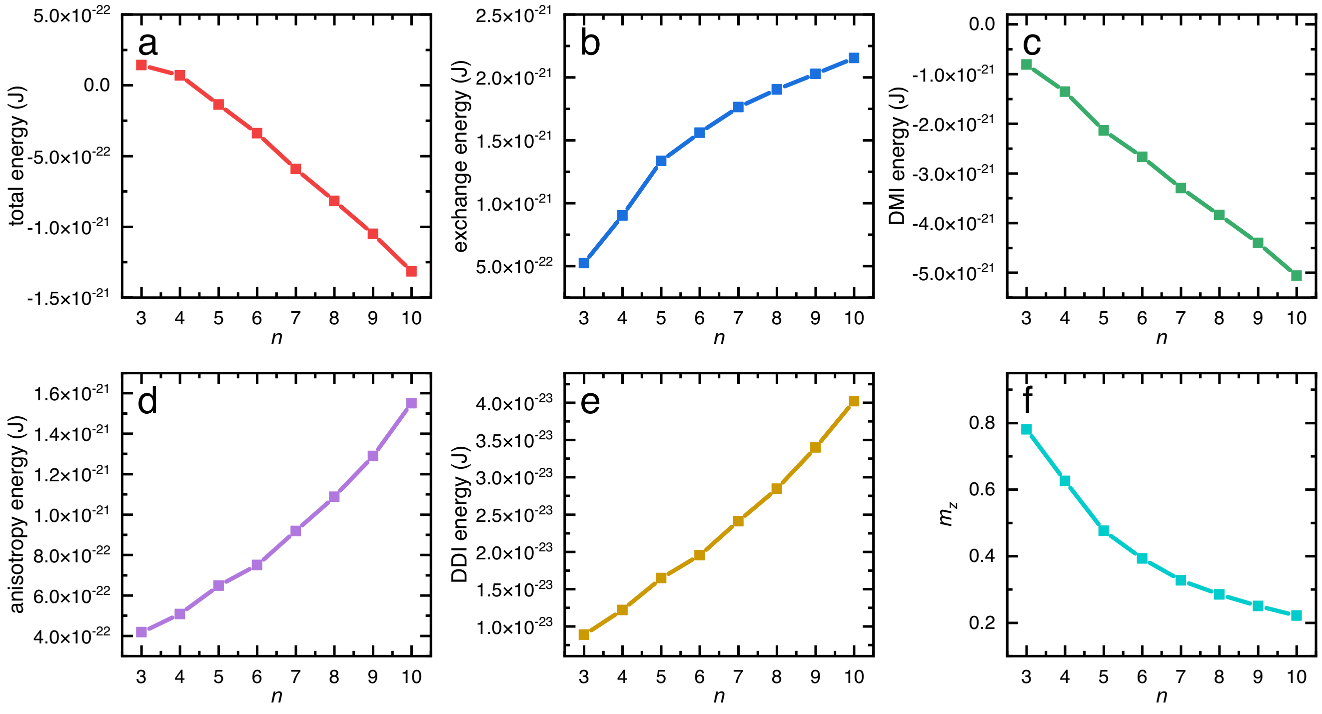

Fig. 7 Size dependence of the energy of the meron in units of Joule. a The total energy. **b** The exchange energy. **c** The DMI energy. **d** The easy-plane magnetic anisotropy energy. **e** The magnetic dipole–dipole energy. **f** The normalized out-of-plane magnetization. The radius of the meron is $n = 7$. The simulation parameters are given in the caption of Fig. 2. More details are given in the "Methods" section.

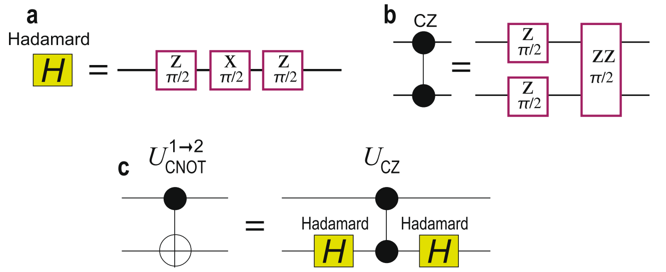

Fig. 8 Quantum circuit representations. a The Hadamard gate in terms of a sequential application of rotation gates as in Eq. (23). **b** The CZ gate in terms of a sequential application of the z rotation gate and the Ising coupling gate U_{ZZ} as in Eq. (28). **c** Quantum circuit representations of the equivalence between the CNOT gate as in Eq. (30) and the CZ gate with the application of the Hadamard gates. $U_{\mathrm{CNOT}}^{1\to 2}$.

In particular, the Pauli-Z gate $U_Z \equiv \sigma_z$ is constructed by setting $\theta = \pi$ as $U_Z = iU_Z(\pi)$.

Pauli-X gate. In a similar way, we set $B_z = 0$ and

$$\alpha_x = \hbar\theta/2t_0 \tag{19}$$

for $0 \le t \le t_0$ and $B_z(t) = 0$ otherwise. The solution of the Schrödinger equation reads

$$U_X(\theta) = \exp\left[-\frac{i}{\hbar}\sigma_x \int_0^{t_0} \alpha_x(t)\mathrm{d}t\right] = \exp\left[-\frac{i\theta}{2}\sigma_x\right]. \tag{20}$$

This is the x rotation gate by the angle θ. The Pauli-X gate $U_X \equiv \sigma_x$ is constructed by setting $\theta = \pi$ as $U_X = iU_X(\pi)$.

***π*/4 phase-shift gate**. The $\pi/4$ phase-shift gate is realized by the z rotation (17) with the angle $-\pi/4$ as

$$U_T = \mathrm{e}^{\mathrm{i}\pi/8} U_Z\left(-\frac{\pi}{4}\right), \tag{21}$$

up to the overall phase factor $\mathrm{e}^{\mathrm{i}\pi/8}$.

Hadamard gate. The Hadamard gate is defined by

$$U_{\mathrm{H}} \equiv \frac{1}{\sqrt{2}}\begin{pmatrix} 1 & 1 \\ 1 & -1 \end{pmatrix}, \tag{22}$$

which is realized by a sequential application of the z rotation and the x rotation[47] as

$$U_{\mathrm{H}} = -iU_Z\left(\frac{\pi}{2}\right)U_X\left(\frac{\pi}{2}\right)U_Z\left(\frac{\pi}{2}\right), \tag{23}$$

with the use of Eqs. (17) and (20). The quantum circuit representation of Eq. (23) is shown in Fig. 8a.

Ising coupling gate. Next, we discuss the two-qubit gate. We manually control d_m as a function of time. Then, the time evolution is given by

$$U = \exp\left[-\frac{i}{\hbar}\int_0^{t_0} H_{\mathrm{Ising}}(d_m(t))\mathrm{d}t\right] \tag{24}$$

with $d_m = d_m(t)$ in Eq. (15). If we set

$$J_{\mathrm{int}}(d_m(t)) = \hbar\theta/2t_0 \tag{25}$$

for $0 \le t \le t_0$ and $J_{\mathrm{int}}(d_m(t)) = 0$ otherwise, we obtain the Ising coupling gate

$$U_{ZZ}(\theta) \equiv \exp\left[-\frac{i\theta}{2}\sigma_z^{(1)}\sigma_z^{(2)}\right], \tag{26}$$

acting on the 2-qubit in the neighboring layers. By setting $\theta = \pi$, we obtain the Ising coupling gate $U_{ZZ} \equiv (1, -1, -1, 1)$ as $U_{ZZ} = iU_{ZZ}(\pi)$.

CZ gate. The controlled-Z (CZ) gate U_{CZ} is a unitary operation acting on two adjacent qubits defined by

$$U_{\mathrm{CZ}} = \mathrm{diag.}(1, 1, 1, -1), \tag{27}$$

and constructed as[48]

$$U_{\mathrm{CZ}} = \mathrm{e}^{\mathrm{i}\pi/4} U_Z^{(1)}\left(\frac{\pi}{2}\right)U_Z^{(2)}\left(\frac{\pi}{2}\right)U_{ZZ}^{(1)}\left(-\frac{\pi}{2}\right), \tag{28}$$

whose quantum circuit representation is shown in Fig. 8b.

CNOT gate. The CNOT gate $U_{\mathrm{CNOT}}^{1\to2}$ is defined by

$$U_{\mathrm{CNOT}}^{1\to2} \equiv \begin{pmatrix} 1 & 0 & 0 & 0 \\ 0 & 1 & 0 & 0 \\ 0 & 0 & 0 & 1 \\ 0 & 0 & 1 & 0 \end{pmatrix}, \tag{29}$$

which is constructed by a sequential application of the CZ gate and the Hadamard gate as

$$U_{\mathrm{CNOT}}^{1\to2} = U_{\mathrm{H}}^{(2)} U_{\mathrm{CZ}} U_{\mathrm{H}}^{(2)}, \tag{30}$$

where the control qubit is the meron in the first layer and the target qubit is the meron in the second layer. The corresponding quantum circuit representation is shown in Fig. 8c.

Data availability

The data that support the findings of this study are available from the corresponding author upon reasonable request.

Code availability

The micromagnetic simulator MuMax is publicly accessible at https://mumax.github.io/index.html. The micromagnetic simulator OOMMF is publicly accessible at https://math.nist.gov/oommf.

Received: 2 June 2022; Accepted: 28 October 2022;

References

1. Feynman, R. Simulating physics with computers. *Int. J. Theor. Phys.* **21**, 467 (1982).
2. DiVincenzo, D. P. Quantum computation. *Science* **270**, 255 (1995).
3. Nielsen, M. & Chuang, I. *Quantum Computation and Quantum Information* (Cambridge University Press, 2016).
4. Deutsch, D. Quantum theory, the Church–Turing principle and the universal quantum computer. *Proc. R. Soc. A* **400**, 97 (1985).
5. Dawson, C. M. & Nielsen, M. A. The Solovay–Kitaev algorithm. Preprint at arXiv: quant-ph/0505030.
6. Nielsen, M. & Chuang, I. *Quantum Computation and Quantum Information* (Cambridge University Press, Cambridge, UK, 2010).
7. Nakamura, Y., Pashkin, Yu. A. & Tsai, J. S. Coherent control of macroscopic quantum states in a single-Cooper-pair box. *Nature* **398**, 786 (1999).
8. Knill, E., Laflamme, R. & Milburn, G. J. A scheme for efficient quantum computation with linear optics. *Nature* **409**, 46 (2001).
9. Loss, D. & DiVincenzo, D. P. Quantum computation with quantum dots. *Phys. Rev. A* **57**, 120 (1998).
10. Cirac, J. I. & Zoller, P. Quantum computations with cold trapped ions. *Phys. Rev. Lett.* **74**, 4091 (1995).
11. Vandersypen, L. M. K. et al. Experimental realization of Shoras quantum factoring algorithm using nuclear magnetic resonance. *Nature* **414**, 883 (2001).
12. Kane, B. E. A silicon-based nuclear spin quantum computer. *Nature* **393**, 133 (1998).
13. Psaroudaki, C. & Panagopoulos, C. Skyrmion qubits: a new class of quantum logic elements based on nanoscale magnetization. *Phys. Rev. Lett.* **127**, 067201 (2021).
14. Xia, J., Zhang, X., Liu, X., Zhou, Y. & Ezawa, M. Universal quantum computation based on nanoscale skyrmion helicity qubits in frustrated magnets. Preprint at arXiv:2204.04589.
15. Bogdanov, A. N. & Yablonskii, D. A. Thermodynamically stable "vortices" in magnetically ordered crystals. The mixed state of magnets. *Sov. Phys. JETP* **68**, 101 (1989).
16. Rößler, U. K., Bogdanov, A. N. & Pfleiderer, C. Spontaneous skyrmion ground states in magnetic metals. *Nature* **442**, 797 (2006).
17. Bogdanov, A. N. & Panagopoulos, C. Physical foundations and basic properties of magnetic skyrmions. *Nat. Rev. Phys.* **2**, 492 (2020).
18. Nagaosa, N. & Tokura, Y. Topological properties and dynamics of magnetic skyrmions. *Nat. Nanotech.* **8**, 899 (2013).
19. Fujishiro, Y., Kanazawa, N. & Tokura, Y. Engineering skyrmions and emergent monopoles in topological spin crystals. *Appl. Phys. Lett.* **116**, 090501 (2020).
20. Tang, J. et al. Two-dimensional characterization of three-dimensional magnetic bubbles in Fe_3Sn_2 nanostructures. *Natl Sci. Rev.* **8**, nwaa200 (2021).
21. Tang, J. et al. Magnetic skyrmion bundles and their current-driven dynamics. *Nat. Nanotechnol.* **16**, 1086 (2021).
22. Zhang, X. et al. Skyrmion-electronics: writing, deleting, reading and processing magnetic skyrmions toward spintronic applications. *J. Phys. Condens. Matter* **32**, 143001 (2020).
23. Kikuchi, N. et al. Vertical bistable switching of spin vortex in a circular magnetic dot. *J. Appl. Phys.* **90**, 6548 (2001).
24. Yamada, K. et al. Electrical switching of the vortex core in a magnetic disk. *Nat. Mater.* **6**, 270 (2007).
25. Bohlens, S. et al. Current controlled random-access memory based on magnetic vortex handedness. *Appl. Phys. Lett.* **93**, 142508 (2008).
26. Hertel, R., Gliga, S., Fahnle, M. & Schneider, C. M. Ultrafast nanomagnetic toggle switching of vortex cores. *Phys. Rev. Lett.* **98**, 117201 (2007).
27. Nakano, K. et al. All-electrical operation of magnetic vortex core memory cell. *Appl. Phys. Lett.* **99**, 262505 (2011).
28. Curcic, M. et al. Polarization selective magnetic vortex dynamics and core reversal in rotating magnetic fields. *Phys. Rev. Lett.* **101**, 197204 (2008).
29. Goto, M. et al. Electric spectroscopy of vortex states and dynamics in magnetic disks. *Phys. Rev. B* **84**, 064406 (2011).
30. Im, M.-Y. et al. Symmetry breaking in the formation of magnetic vortex states in a permalloy nanodisk. *Nat. Commun.* **3**, 983 (2012).
31. Uhlir, V. et al. Dynamic switching of the spin circulation in tapered magnetic nanodisks. *Nat. Nanotech* **8**, 341 (2013).
32. Wintz, S. et al. *Phys. Rev. Lett.* **110**, 177201 (2013).
33. Siracusano, G. et al. Topology and origin of effective spin meron pairs in ferromagnetic multilayer elements. *Phys. Rev. Lett.* **117**, 087204 (2016).
34. Okuno, T., Shigeto, K., Ono, T., Mibu, K. & Shinjo, T. MFM study of magnetic vortex cores in circular permalloy dots: behavior in external field. *J. Magn. Magn. Mater.* **240**, 1 (2002).
35. Van Waeyenberge, B. et al. Magnetic vortex core reversal by excitation with short bursts of an alternating field. *Nature* **444**, 461 (2006).
36. Kim, S.-K., Choi, Y.-S., Lee, K.-S., Guslienko, K. Y. & Jeong, D.-E. Electric-current-driven vortex-core reversal in soft magnetic nanodots. *Appl. Phys. Lett.* **91**, 082506 (2007).
37. Shekaa, D. D. Current induced switching of vortex polarity in magnetic nanodisks. *Appl. Phys. Lett.* **91**, 082509 (2007).
38. Curcic, M. et al. Polarization selective magnetic vortex dynamics and core reversal in rotating magnetic fields. *Phys. Rev. Lett.* **101**, 197204 (2008).
39. Kima, S.-K., Lee, K.-S., Yu, Y.-S. & Choi, Y.-S. Reliable low-power control of ultrafast vortex-core switching with the selectivity in an array of vortex states by in-plane circular-rotational magnetic fields and spin-polarized currents. *Appl. Phys. Lett.* **92**, 022509 (2008).
40. Kamionka, T. et al. Magnetic antivortex-core reversal by rotating magnetic fields. *Phys. Rev. B* **83**, 224422 (2011).
41. Jin, W., He, H., Chen, Y. & Liu, Y. Controllable vortex polarity switching by spin polarized current. *J. Appl. Phys.* **105**, 013906 (2009).
42. Caputo, J.-G., Gaididei, Y., Mertens, F. G. & Sheka, D. D. Vortex polarity switching by a spin-polarized current. *Phys. Rev. Lett.* **98**, 056604 (2007).
43. Wachowiak, A. et al. Direct observation of internal spin structure of magnetic vortex cores. *Science* **298**, 577 (2002).
44. Kasai, S. et al. Three-terminal device based on the current-induced magnetic vortex dynamics with the magnetic tunnel junction. *Appl. Phys. Express* **1**, 091302 (2008).
45. Vansteenkiste, A. et al. The design and verification of MuMax3. *AIP Adv* **4**, 107133 (2014).
46. Donahue, M. J. & Porter, D. G. *OOMMF User's Guide, Version 1.0.* Interagency Report No. NISTIR 6376 (National Institute of Standards and Technology, Gaithersburg, MD, 1999).
47. Schuch, N. & Seiwert, J. Natural two-qubit gate for quantum computation using the XY interaction. *Phys. Rev. A* **67**, 032301 (2003).
48. Makhlin, Y. Nonlocal properties of two-qubit gates and mixed states and optimization of quantum computations. *Quantum Inf. Process.* **1**, 243 (2002).

Acknowledgements

M.E. is very much grateful to N. Nagaosa for helpful discussions on the subject. This work is supported by the Grants-in-Aid for Scientific Research from JSPS KAKENHI (Grant No. JP18H03676). This work is also supported by CREST, JST (Grant No. JPMJCR20T2). J.X. was a JSPS International Research Fellow supported by JSPS KAKENHI (Grant No. JP22F22061). X.L. acknowledges support by the Grants-in-Aid for Scientific Research from JSPS KAKENHI (Grant Nos. JP21H01364, JP21K18872, and JP22F22061). Y.Z. acknowledges support by the Guangdong Basic and Applied Basic Research Foundation (Grant No. 2021B1515120047), Guangdong Special

Support Project (Grant No. 2019BT02X030), Shenzhen Fundamental Research Fund (Grant No. JCYJ20210324120213037), Shenzhen Peacock Group Plan (Grant No. KQTD20180413181702403), Pearl River Recruitment Program of Talents (Grant No. 2017GC010293), and the National Natural Science Foundation of China (Grant Nos. 11974298, 12004320, and 61961136006).

Author contributions

M.E. conceived the idea and conducted the project. M.E. carried out the theoretical analysis. J.X. and X.Z. performed numerical simulations in collaboration with X.L. and Y.Z. All authors discussed the results and wrote the manuscript.

Competing interests

The authors declare no competing interests.

Additional information

Correspondence and requests for materials should be addressed to Motohiko Ezawa.

Peer review information *Communications Materials* thanks the anonymous reviewers for their contribution to the peer review of this work. Primary Handling Editor: Aldo Isidori.